Fine-Scale Three Dimensional Mapping of a Deep-Sea Hydrothermal Vent Site Using the Jason ROV System

Dana R. Yoerger
Deep Submergence Laboratory
Dept. of Applied Ocean Physics and Engineering
Woods Hole Oceanographic Institution
Woods Hole, MA 02543

Deborah S. Kelley
John R. Delaney
School of Oceanography
Box 357940
University of Washington
Seattle, WA 98195-7940

Abstract

Using precise navigation, a computer-controlled remotely operated vehicle, and a variety of optical and acoustic imaging sensors, we created the most precise three-dimensional renderings ever made of an active hydrothermal vent field at a depth of 2400 meters on the deep-sea floor. Data products included electronic and film photographs as well as three-dimensional sonar scans. We used these to produce detailed photomosaics and gridded surface renderings. Precise navigation and control of the vehicle during all transects permitted us to register all observations in a common world frame, ensured complete and uniform coverage, and allowed biases to be identified and removed. The assembled photomosaics and sonar renderings provide valuable insights into the unique environment of submarine hydrothermal vents.

1. Introduction

The discovery of high-temperature hydrothermal vents in the deep ocean can be counted as one of the most important and exciting discoveries of the past century. Fueled by heat from magma chambers and hot rock lying beneath the mid-ocean ridges, these underwater hot springs, which reach temperatures in excess of 400C (Humphris 1995, Delaney 1992), provide answers to unsolved questions regarding the heat balance of the earth and the chemical balance of the world's oceans. Investigations of vents with tow sleds and manned submersibles also revealed a startling discovery: the vents support vibrant ecosystems featuring a variety of previously unknown life forms. In these communities, chemosynthetic microbes convert chemical energy from the gas-laden vent fluids into biologically available energy; much as green plants convert sunlight through photosynthesis. These heat-loving single celled organisms, known as hyperthermophiles, are believed to represent the most ancient of extant organisms on earth (Karl, 1995, Baross 1993).

Following discovery of the first vents in 1977, demand for routine access to the deep seafloor increased dramatically (Ballard 2000b). Tow sleds such as the Woods Hole Oceanographic Institution's ANGUS and the Scripps Institute for Oceanography's Deep-Tow discovered additional hydrothermal vents. Manned submersibles such as Alvin allowed scientists to directly observe and document vent systems and to establish their geologic context. In addition, these research platforms allowed unprecedented direct sampling of the mineral deposits, animals, microbes, and vent fluids, and allowed in-situ experiments to be performed. In the 1990s, remotely operated vehicles and tow sleds linked to the surface with fiber-optic cables began providing remote access with improved endurance and superior fine-scale mapping capabilities.

In addition to their importance as sources of heat and chemical energy that support diverse biological communities on the seafloor, vents serve as windows to a complex and poorly understood environment beneath the seafloor. The fluids feeding vents travel deep within the earth, dissolving minerals and responding to a variety of phenomena such as earthquakes, volcanic eruptions, and even tidal forcing of the ocean and earth's crust (Fornari, 1995; Delaney, 1997). Through iterative hypothesis testing, scientists are beginning to unravel the complex relationships between fluid flow, geochemistry, and microbial life. Increasingly, scientific consensus is building that the microbial life found in and around vents could be the surface expression of vast, complex anaerobic microbial ecosystems within the earth's crust. Some scientists hypothesize that the submarine subsurface biosphere may rival the earth's terrestrial ecosystems in terms of total biomass. Others hypothesize that such vents, with their accompanying microbial ecosystems, could be found elsewhere in our solar system and may have given rise to the first life on Earth.

In September 1997, as part of an investigation to understand geo-biological processes active within vent environments, we mapped a subsea hydrothermal field known as Mothra using the Remotely Operated Vehicle Jason (Ballard 1993) shown in figure 1. The Mothra Field (MHF), located at the Juan de Fuca Ridge off the Washington coast, consists of rugged volcanic terrain and multiple isolated tall sulfide pinnacles. These spires are awash in superheated, mineral-laden fluid from so-called "black smoker" vents, which reach temperatures of 300C. Sonar maps and photomosaics encompassed an area approximately 100 meters by 40 meters with high precision and detail, providing a context for a variety of multidisciplinary investigations. This mapping effort was the first stage of an ambitious project called Edifice Rex, conducted by geologists from the University of Washington and the American Museum of Natural History (Delaney, 2000; Kelley, 1997, Yoerger 1999b). Based on this mapping effort, during the follow-on field season the top two meters of four hydrothermal chimneys weighing 4000 lbs. each, were recovered from this area using the Canadian remotely operated vehicle ROPOS (Kelley, 1999; Delaney, 2000).

Similar to our archaeological work on ancient deep-sea shipwrecks (Ballard 2000a), we mapped the venting area with sonar and cameras before sampling disturbed it. Unlike the ancient shipwreck sites and other more recent wrecks surveyed by ROV (Stewart 1991), the hydrothermal site was larger and contained vigorous 300C vents, it was in >2300 m of water at the edge of a large fault scarp, and was highly complex and three-dimensional. These additional constraints required that we significantly expand our navigational reference system, map in both down looking and forward looking mode, and sustain our mapping effort for many days. After gathering the data, we had to manage a much larger data set, remove systematic errors from data obtained over three dives and many survey tracks, and we had to combine three dimensional data gathered from different perspectives.

Mothra is one of four well-mapped vigorously venting hydrothermal fields along the axial valley of the Endeavour Segment on the northern end of the Juan de Fuca Ridge. The MHF is comprised of at least five active clusters of sulfide structures that extend 500 m along the base of the west wall of the axial valley. In 1997, we mapped two of these clusters, Twin Peaks and Faulty Towers, to decimeter resolution using the remotely operated vehicle Jason. A third cluster, Crab Basin, was imaged digitally but not well surveyed. The three areas, spaced 50-70 m apart, are bounded to the west by talus off the western axial valley wall and to the east by a collapse basin associated with axial valley floor formation. Initial dive observations of the Faulty Towers and Crab Basin clusters showed abundant, isolated steep sided sulfide pinnacles and these two areas became the focus of the mapping and sulfide recovery effort (figure 2).

More than 13 large sulfide pinnacles occur in the Faulty Towers complex, the two tallest of which The Tower and Giraffe reach 22-24 meters in height. The outer surfaces of the actively venting structures are bathed in a buoyant, shimmering mixture of seawater and outward-diffusing vent fluids. Because of the high fluid output, the outer surfaces of these structures are overgrown with dense macrofaunal vent communities of tube worms, limpets, snails, and crabs. The growth and collapse of these structures is evidenced by a steep 6 m high sulfide talus mound that underlies the large edifices, and by the presence of relatively intact fallen sulfide spires that litter the basin to the west. Three active black smoker chimneys venting fluids up to 302C occur as parasitic overgrowths on the adjacent larger, diffusely venting edifices. Two of these are located at the northern end of the cluster, and a third free standing vent, Finn, is located near a small saddle at the southern terminus adjacent to the structures Roane and Phang (figure 2).

To investigate the evolution of sulfide growth and associated microbiological activity, structures covering a spectrum of vent activity were chosen for recovery; they include Finn, a robust 300C black smoker, Roane and Gwenen which are dominated by diffuse <200C output and dense macrofaunal communities, and Phang, an extinct edifice. These sulfide structures, which are habitats for diverse microbial populations that grow in excess of 90C, are the subject of intense, multidisciplinary study and portions of them are on public display at the American Museum of Natural History in New York.

2. Mapping Technique

We exploited the Jason ROV system's precise, centimeter-scale navigation and automated control to create fine-scale resolution three-dimensional maps of the sulfide structures and surrounding terrain. Given precise knowledge of the ROV position and orientation, we transformed individual returns from a pencil-beam scanning sonar into world coordinates to form a three-dimensional representation of the geological structures. Simultaneously, we collected imaging data from a variety of electronic and film cameras, which we assembled into mosaics of the structures. By precisely controlling vehicle motion, the resulting electronic camera images could be more easily mosaicked as image overlap remained constant and the viewpoint moved in only one dimension over each track segment. Careful planning of each track segment, or transect, was required to obtain coverage while maintaining a clear line of site from the navigation transducer on the vehicle to at least two transponders.

We executed 115 precise, automatically controlled transects with the imaging sensors directed forward (83 transects) and down (29 transects) over a series of three dives. Over the three dives, Jason spent 64 hours working on the seafloor.

The precision of the automated transects proved extremely valuable. The automatic control capability permitted us to survey systematically with consistent coverage. Also, the desired survey speed for the digitizing sonar was slower than could be maintained by a human pilot but could be easily achieved by the control system. Finally, precisely controlled, straight-line transects permitted systematic biases to be computed analytically and removed from the sonar records (Singh 2000), and also enabling simplified gridding.

2.1 Navigation

Major elements of the navigation sensor suite included a fluxgate magnetic compass (KVH C100), a free gyro (Humphries DG78), inclinometers (Shaevitz Accustar), and a pressure depth sensor (Paroscientific 410KT), a broadband 300 kHz acoustic transponder system (Marquest Exact), and a 1200 kHz. acoustic doppler navigator (RDI WHN-1200).

Due to the unavailability of a suitable north-seeking gyrocompass, Jason carries two heading sensors, both of which have intrinsic shortcomings. The fluxgate compass has a sluggish dynamic response and can be corrupted by magnetic anomalies. The rate gyro has no sense of absolute heading and drifts at a rate of approximately 6 degrees per hour. These characteristics are not completely complementary; low frequency errors induced in the fluxgate by magnetic influence of the local geology were not observable due to the drift of the gyro.

Inclinometers measure Jason's pitch and roll. These units have linearity of 0.1 degrees in Jason's operating range, although they must be carefully calibrated to determine their offsets.

Jason's depth is measured by a precision pressure sensor, which operates in a mode that provides a resolution of 1.5 cm with updates every 0.8 second. As pressure depth provides a reference to the sea surface rather than a frame fixed to the seafloor, tidal effects make up the dominant errors in the estimate of vertical position.

Our technique for determining the position of the vehicle relies on a combination of high-frequency transponders and bottom-lock doppler sonar (Whitcomb 1998, Whitcomb 1999b).

Absolute position was determined by measuring ranges from two 300 kHz broadband transponders (Exact) placed on the seafloor combined with the measured depth. These transponders have a range precision of

approximately 1 cm. (Yoerger 1999a)

For the ranges from the transponders to be transformed into valid cartesian coordinates, the relative transponder positions must be known. Net survey proceeded in several steps. The depths of each transponder were measured by Jason's depth sensor when the units were placed on the seafloor. The range between transponders was measured by a "sing around" technique that has precision comparable to the range measurements. The position and orientation of the first two Exact transponders were placed in world coordinates (translation and rotation) by referencing Jason's low frequency transponder (LBL) net. After the first two Exact transponders were referenced to the LBL net, subsequent transponders were surveyed relative to previously surveyed transponders, thus maintaining high internal precision. As the Exact system supports only four transponders, we moved transponders several times to achieve the needed coverage.

Positions were computed by measuring ranges from two transponders; each interrogated separately twice per second. Travel times were converted to ranges with a single speed-of-sound estimate based on measured depth and estimates of temperature and salinity. A 5-point median filter rejected spurious ranges. Fixes were computed by first projecting range measurements into a plane using depth measurements, then triangulating a 2D fix with the baseline side entered manually. Relative motion of the ROV was measured with a 1200 kHz bottom-lock doppler navigator. This device uses four acoustic beams to measure the vehicle velocity relative to the seafloor, transforms the velocities into world coordinates using its own internal fluxgate compass and inclinometers, then integrates the velocities to produce displacements.

These two positioning sensors form a fully complementary set of measurements. The transponders provide highly precise absolute positioning relative to the defined net, but the update rate is limited and measurements can be susceptible to dropouts and spurious returns. The doppler navigator (DVL) has an excellent dynamic response and maintained bottom lock over a variety of bottom types, but provides a position estimate that contains a low but unpredictable drift. In addition to the influence of velocity errors the DVL and transponder position measurements will diverge due to rotation errors.

We combined the two position references in real-time with a classical first-order complementary filter (Lin, 1991) using a time constant of 5 seconds. This filter leveraged the drift-free nature of the transponder fixes while taking full advantage of the excellent dynamic response of the DVL. Likewise, the filter mitigated the effect of transponder dropouts and DVL drift. Real time and post-processing of the navigation data is summarized in figure 3.

While we have no independent method for verifying the precision of our navigation suite (no other comparable system was available), we have confidence in our results for the following reasons:

1. The acoustic time-of-flight measurements were determined using a time base accurate to approximately 1 part in 10^5.
2. Our estimate of the speed of sound in water, based on measurements of pressure and estimates of temperature and salinity, was accurate to at least one part in 10^3
3. The "sing around" calibration method provides the distance between each transponder pair with precision consistent with the other range measurements (1 cm).

Errors in the estimate of transponder baseline distance are the most critical, as they would produce a "warping" of the navigation fixes relative to true cartesian coordinates. Stable errors in the time base or the sound speed estimate would result in a scaling error. As an overall confirmation of the precision of the position estimates, we will show later that the resulting sonar swaths match up well after correction for attitude biases and tidal variations. No adjustment for the position estimates was required.

2.2 Automatic control

Jason's automatic systems controlled the vehicle's heading, depth, and horizontal position. The heading loop was closed using feedback from the gyro, which was reset to the fluxgate compass value at the start of each transect. Vehicle depth was controlled using the precision depth measurement, with a depth rate extracted by differentiation with light filtering. Vehicle position was controlled based on position estimates from the real-time complementary filter.

We designed Jason's automatic control system to assist rather than replace the human pilot. Rather than entering a sequence of automated moves, the pilot can enter a single relative move (e.g. forward 5 meters or north 5 meters) at a prescribed speed (e.g. 2 cm/sec) through a button box. This command generates a smooth reference trajectory at the desired speed, while commanded values on the other axes remain constant. Commands can be entered for heading, depth, or horizontal position. A movement can be cancelled at any time, in which case the vehicle holds position. Likewise, the speed can be adjusted at any time.

After the start of a move along one axis, adjustments can be made on other axes. For example, while executing a long horizontal translation, the pilot can adjust the depth to maintain proper sensor offset from the seafloor. Representative down-looking and forward-looking trajectories around the Faulty Towers structures are shown in figure 4.

The automatic controls and interactive command interface were especially effective while maneuvering in areas of high relief. Despite our fears of entangling or even severing the tether in the superheated plumes, we obtained good coverage over and around the 20-meter tall sulfide spires without incident. Using the interactive controls during down-looking transects, the pilot was able to maneuver the vehicle very close to the spires, stop forward motion, change depth to reach a safe height above the tops of the spires, maneuver over the top, then safely descend on the other side. As the pilot was not burdened by manually controlling vehicle position, he was able to take full advantage of feedback from all cameras as well as the scanning sonar. These inputs permitted the pilot to maintain proper sensor offset without jeopardizing the safety of the vehicle.

2. 3 Imaging Sensors

High quality color video was provided by a Panasonic WVE550 (3 chip camera), custom packaged, with water corrected optics. Both incandescent (1000 watts) and HMI (1200 watts) units provided lighting.

A Marquest 8100 Electronic Still Camera (ESC) was used to collect monochrome images. The resolution of this device is 576x384. Images were taken every 13 seconds and could be viewed as they were transmitted to the surface.

We used an Imagenix model 855 mechanically scanned pencil-beam sonar to collect range data. The unit operates at 675 kHz with a 1.9-degree conical beam, steps in 1.2-degree increments, and moves at approximately 2 steps/second depending on range. Full analog returns were shown in real time on the standard Imagenix display. The range digitization threshold was adjusted manually, and only digitized ranges (one per ping) were recorded digitally.

We used two sensor configurations, forward looking and down looking. In each case, the sonar was positioned so that it scanned through the center of the field of the ESC and the 3-chip color video camera.

2.4 Transect Planning and Execution

Transect planning made up a critical element of the survey. The watch leader had responsibility for obtaining complete, even coverage with substantial overlap. Transponder coverage issues complicated transect selection, during each transect continuous line-of-sight had to be maintained to at least two transponders with good geometry. We reference each Jason dive by a number representing the total number of dives to

date.

Jason Dive 229

For the first dive, Jason 229, the imaging sensors were configured in the forward-looking mode. We executed 56 transects over a period of 34 hours. These transects were run with the vehicle primarily at a fixed horizontal position and moving vertically at a speed of 2 cm/sec. These transects concentrated on the southern or Faulty Towers group of structures. The watch leader guided the pilot; ensuring overlap of camera coverage between transects. Sometimes, the optimal heading and positioning of a transect from a coverage perspective could not be achieved while maintaining line-of-sight to the transponders or due to transponder net geometric considerations. Three different transponder pairs were used; one of which was moved once and resurveyed.

Each transect covered a vertical translation of approximately 20 meters and took about 20 minutes. The ROV pilot commanded small horizontal motions to maintain a nominal distance of 4 meters from the structures.

Some transects from this dive were directed toward video coverage not quantitative sonar and imaging. Of the 56 transects from this dive, 21 were included in the final sonar map. We obtained good coverage all around the structures with the exception of the southern end due to transponder coverage difficulties.

Jason Dive 230

For the second dive, Jason 230, the imaging sensors were configured looking down. On this dive, we covered both the Faulty Towers and the northern Twin Peaks sites at a nominal distance of 4 meters from the bottom. A total of 29 transects were executed, each taking about 25 minutes when the underlying terrain was fairly benign. When passing directly over the tall structures, the time to complete a transect could double. Total time spent running transects was 19.5 hours. In the Faulty Towers area, 4 transponders were used in two pairs. After moving two of the transponders, a similar setup was used on the Twin Peaks site.

For each area, all transects were made at the same heading regardless of the direction of travel. This ensured consistent line of sight to the transponders and reduced the influence of biases. Of the 29 transects made, 18 were included in the final sonar map. We obtained complete, linked down-looking coverage of both areas.

Jason Dive 231

For the third and final dive, Jason 231, the imaging sensors were again configured forward in order to survey the northern or Twin Peaks field. A total of 28 transects were run, again maintaining the 2 cm/sec vertical speed. As these structures were shorter than those at the southern field, transects took about 8 minutes each. 10.3 hours were spent running transects. Three transponders were used; one of which was moved and resurveyed. The dive was terminated early due to bad weather, preventing us from filling in a few gaps at the southern end of Faulty Towers.

3. Sonar Processing

The objective of the navigation and sonar post-processing was to transform the range and bearing measurements from the scanning sonar into a "dot cloud" of points registered in world coordinates. From these "dots", a number of techniques can be used to create three-dimensional surfaces.

The surfaces were sampled as finely as possible given constraints on the sonar performance, scanning speed, and tight schedule. Given the goal of maintaining a 4-5 meter offset from the target (consistent with obtaining electronic still imagery) and the assigned vertical speed of 0.02 meters/second, we obtain mean spacing between "dots" of approximately 0.1 meters in both the horizontal and vertical directions. As described by Stewart (1990), these "dots" can be interpreted by considering the intersection of the sonar beam pattern with the surface.

3.1 Navigation post-processing technique

We improved our estimate of the vehicle position by post-processing. By working with the full data set, we could better reject bad ranges, recover more good ranges, further reduce doppler drift, and interpolate through transponder dropouts.

Figure 5 shows an example of the navigation process. The upper plot shows the raw transponder navigation fixes on one axis along with the doppler position estimate (displaced by 5 meters for clarity). A few bad fixes were obtained, as systematic erroneous ranges can pass through the real-time median filters. Likewise, periods with no transponder fixes can be seen. These computations are summarized in figure 3. The DVL

track varies from the transponder track due to both drift and angular misalignment. Both these problems were dramatically reduced using a zero-phase, off-line complementary filter.

3.2 Initial Sonar Processing

The sonar range and bearing measurements for each transect were transformed into world coordinates (Whitcomb 1997). This process involves first interpolating the navigation, attitude, and sonar data onto a common time base, then transforming the sonar data first from sensor into vehicle coordinates, and finally into world coordinates.

3.3 Improved mapping with automatic control

Figure 6 shows "dot clouds" produced by transforming individual range measurements into world coordinates. In addition to illustrating this initial processing, the figure also emphasizes the importance of Jason's automatic control system. The left hand panel shows results from a transect flown manually by a skilled, experienced pilot while the right panel shows a similar transect run with full automatic control. For the automatic case, the precise horizontal position control combined with steady, slow, vertical speed produces a much more uniform pattern of "dots", which will in turn produce a superior surface rendering.

3.4 Corrections for orientation biases and tides

Individual transects required several types of corrections before they could be assembled into a complete "dot cloud". The most significant errors were caused by biases in attitude measurements (Singh, 1999). These biases were anticipated, and we had taken steps to permit them to be extracted from the data. As an example, consider roll angle. Several sources of bias can occur between the electrical measurement of roll and the actual roll of the transducer head, including alignment of the roll sensor on the chassis, chassis in the pressure housing, pressure housing on the vehicle, and sensor head on the vehicle. We make every attempt to estimate these accurately, but also make specific transects with the vehicle, leveraging Jason's automatic control capabilities, that allow us to observe these biases.

Figure 7 shows an example used to determine roll bias. Over a gently changing bottom, the vehicle was commanded to move sideways at a very slow speed. Before the roll bias was deduced, the resulting dot cloud, as viewed from behind the vehicle, is tilted and contains substantial scatter (top trace of figure 7). We first developed an error metric for consistency. The processed sonar readings were projected into a vertical

plane parallel to the vehicle track. Then, a spatial high-pass filter was applied to remove systematic changes due to the shape of the seafloor. To implement the high-pass filter on the non-uniformly sampled data, the displacement along the vehicle track was divided into a number of bins (50), and the mean of each bin was removed. The standard deviation of the data in each bin was computed then summed across all bins. Numerical minimization then produced a value of roll bias coinciding to the sharpest profile that also contains accurate slopes. The results after minimization are shown at the top of figure 7. A similar technique applied to heading determined the offset between heading measured by the fluxgate compass and the XY coordinate frame of the transponder navigation. The error criteria and minimization procedure are summarized in figure 8.

Tidal effects directly influenced our estimate of the vehicle z coordinate. In real-time, we periodically returned the vehicle to reference stations. This process was time-consuming and awkward. In post-processing, we were able to remove most tidal effects by exploiting overlap in transects and did not use the reference data. Figure 9 shows a vertical slice of uncorrected and corrected down-looking transects. The same error metric described in the earlier roll example formed the basis of the correction. A single depth offset was computed for each transect.

3.5 Gridding and surface generation

Determining a three-dimensional surface from a collection of points is a well-studied problem, see for example (Edelsbruner, 1994, Hoppe 1994). Solutions have been demonstrated using high-quality data sets for many types of surfaces. However, the sonar data gathered in this survey has several key weaknesses compared to the data considered in most studies. Our data is nonuniformly scanned, noisy, and contains substantial gaps where sonar coverage could not be obtained (behind the smaller, flanking spires or between the spires, for example). On the positive side, we collected our data along carefully controlled transects, which gives each transect's "dot cloud" a two-dimensional character that we can exploit.

Processing of the down-looking data was straightforward, except for the tall structures, which were trimmed out since the forward-looking transects covered them much better. Otherwise, the surface z coordinate is unique at any xy position for the down-looking data. By retaining a two-dimensional representation, spatial filtering and triangularization are greatly simplified. Data from down looking transects were gridded at 0.2 meter intervals using a gaussian kernel with a one-sigma value of 1/2 the grid spacing.

Processing the forward-looking data required additional steps. The structures do not lend themselves to

standard gridding, as the faces are near vertical with numerous overhanging features (called flanges). Since the data was gathered during precisely controlled vertical transects, the data retains a two-dimensional character if viewed in cylindrical coordinates. As shown in figure 10, by processing in cylindrical coordinates, the natural geometry of the sensing process, we avoid smearing overlapping structures.

Figure 11 shows the processing steps for a single vertical transect. The upper left panel shows the raw dot cloud, with false color indicating depth. The upper right panel shows data transformed into cylindrical coordinates with color indicating radial distance. The lower left panel shows the resulting triangulated, segmented surface also in cylindrical coordinates. Segmentation was achieved by simply clipping any triangular facets whose cylindrical span exceeded a preset maximum. The lower right panel shows the resulting surface enhanced by an illumination model.

Figure 12 shows a gridded rendering of the Faulty Towers site as viewed from the east. This image was produced from 8 individual forward-looking transects. These views emphasize the three-dimensional character of the tower, including the nose-like "flange" structure.

4 Photomosaicking

When debating the relative merits of remotely operated vehicles versus manned submersibles, scientists often make the claim "I have to see it for myself". While many regard video as a poor substitute for direct viewing, the precise control and imaging capabilities of an ROV like Jason allow us to create much larger images than can be directly viewed. Attenuation and scattering of light, limited lighting power, camera sensitivity, dynamic range and resolution all limit the size of individual images we can produce underwater. Photomosaicking allows us to build large area images that are physically impossible to view as a single image with either cameras or the human eye.

Before mosaicking, all electronic still images were batch processed to correct camera artifacts and to reduce the effects of uneven lighting within and between images. These steps include corrections for flat field and chip gain effects followed by adaptive histogram equalization. These preprocessing steps create images where background and foreground images appear evenly illuminated.

Finally, images were mosaicked. A commercially available program (Intergraph Base Imager) was employed. Depending on the complexity of the scene, a variety of image warps and blending techniques could be used. These techniques have been developed for use on deep-sea images for a variety of applications

including geology, deep-sea shipwreck forensic studies, and underwater archaeology (Howland 1999).

Figure 13 shows a photomosaic of the east face of Faulty Towers assembled from 67 electronic still camera images gathered during the vertical transects. The photomosaic shows good agreement with the sonar images, reveals the surface structure in much more detail, and additionally shows many active plumes. This comprehensive view of the structure would be impossible to see from the view port of a submersible or from a single camera view.

Figure 14 shows several different renderings of the Twin Peaks site, located about 50 meters to the north of Faulty Towers. The sonar image utilizes both forward-looking and down-looking transects. The photomosaic on the left was assembled from over 20 electronic still camera images. Another example from 7 digitized film images is also shown in figure 14. Due to the precise control of the vehicle and the simplicity of the scene, this mosaic required only translation and blending of the images from a single vehicle transect.

Figure 15 shows east and west views of the Faulty Towers and Twin Peaks sulfide complexes in the northern part of the MHF. These renderings were assembled from 34 vertical transects and 18 horizontal transects and help to delineate many of the geological features within the field. The tall, linear arrays of steep sided pinnacles are oriented parallel to the major volcanic features in this area and they are bounded to the east by a collapsed lava basin associated with formation of the valley which hosts them. Small shallow basins, filled with oxidized hydrothermal sediment expelled from the black smokers, lie to the east and west of the sulfide edifices. Also shown in the images of the Faulty Towers complex is a 6-m tall sulfide rampart that forms the base of the structures. Blocks of sulfide talus and pillow basalts define the rough topography to the south of this area. To the north of Twin Peaks there are two small pillow ridges, the most eastern of which hosts a diffuse flow site colonized by abundant tube worms.

5. Conclusion

Using precise navigation, a computer-controlled remotely operated vehicle, and a variety of optical and acoustic imaging sensors, we created precise three-dimensional renderings of an active hydrothermal vent field at a depth of 2400 meters on the deep-sea floor. Data products included electronic and film photographs as well as three-dimensional sonar scans. We used these to produce detailed photomosaics and gridded three-dimensional surface renderings. Precise navigation and control of the vehicle permitted uniform, even sensor coverage, allowed systematic biases to be determined analytically, and simplified the generation of photomosaics and sonar renderings.

Detailed images such as those produced during this project provide valuable insights into the unique environment of submarine hydrothermal vents. Intense, high resolution imaging of these environments yields important information about the relationships among sulfide structures and the diverse biological communities that they support. Animals such as tube worms; limpets and snails depend on the warm, nutrient-rich fluids that issue from the walls and tops of the chimneys for their survival. High-resolution imagery provides critical information not only on the specific animals that form the vent communities, but also on how the populations evolve due to changes in temperature, fluid chemistry, and hydrothermal flow. Finally, investigation of these systems is providing new insights into microbiological communities that thrive within the walls of the sulfide structures. Indeed, many microorganisms recovered from these environments are hyperthermophilic Archaea, which optimally grow at temperatures in excess of 80C. Recent work on these organisms shows that they may be among the most ancient of extant organisms and may yield information on the origins of life. High intensity mapping and imaging studies of submarine systems over decadal scales, coupled with co-registered sampling investigations, will provide critical insights into the linkages between deep-sea volcanoes and the life they support.

Acknowledgements

We would like to thank the crew of RV Atlantis and WHOI's Deep Submergence Operations Group for their efforts in support of this work. Mitchell Elend of the University of Washington created the photomosaics. Sponsors include the American Museum of Natural History, through University of Washington subcontract 540408 and the National Science Foundation OCE 9627160. This paper is Woods Hole Oceanographic Institution contribution #10250

References

Ballard, R.D., The Medea/Jason remotely operated vehicle system, Deep Sea Research I, vol 40, no. 8, p 1673-1687, 1993.

Ballard, R.D., McCann, A. M., Yoerger, D.R., Whitcomb, L.L., Mindell, D.A., Oleson, J., Singh, H., Foley, B., Adams, J., and Piechota, D. 2000a, The Discovery of Ancient History in the Deep Sea Using Advanced Deep Submergence Technology, Deep Sea Research I, 47, pp1591-1620.

Ballard, R.D. 2000b, The Eternal Darkness, Princeton University Press, 2000,

Delaney, J.R., D.S. Kelley, M.D. Lilley, D.A. Butterfield, R.E. McDuff, J.A. Baross, Deming, J.W, Johnson, H.P., Robigou, V. 1997, The Endeavour Hydrothermal System I: Cellular circulation above an

active cracking front yields large sulfide structures, “fresh” vent water, and hyperthermophilic archaea. RIDGE Events 8: 11–19.

Delaney, J. R., Kelley, D. S., Mathez, E., Yoerger, D., Baross, J., Schrenk, M. 2000, Edifice Rex Sulfide Recovery Project: Interdisciplinary Dissection and Analysis of a Sulfide-Microbial Habitat from a Submarine Hydrothermal System, EoS Transactions, Amer Geophys. Union, Vol 79, No 45, Nov 1998.

Deming, J.W. and Baross, J.A., 1993, Deep-sea smokers: Windows to a subsurface biosphere. Geochimica Cosmochimica Acta, v. 57, 3219-3230.

Edelsbrunner, H., Mucke, E.P. 1994, Three-dimensional alpha shapes, ACM Trans. Graphics 13m 1994, 43-72.

Fornari, D., Embley, R.W. 1995, Tectonic and volcanic controls on hydrothermal processes at the mid-ocean ridges: An overview based on near-bottom and submersible studies, in Humphris, S., J. Lupton, R. Zierenberg, L. Mullineaux, and R. Thomson (eds.), Seafloor Hydrothermal Systems, Am. Geophys. Mon. 91, 1-46.

Hoppe, H. 1994, Surface reconstruction from unorganized points. PhD Thesis, Dept. of Computer Sci. and Eng., Univ. of Washington, June 1994.

Howland, J., Singh, H., Marra, M., Potter, D., 1999 Digital mosaicking of underwater imagery, Sea Tech., Vol 40 no. 6, June 1999

Humphris, S., J. Lupton, R. Zierenberg, L. Mullineaux, and R. Thomson (eds.), Seafloor Hydrothermal Systems, Am. Geophys. Mon. 91, 1995

Kelley, D.S., Delaney, J.R., Yoerger, D.R., Mathez, E.A. 1998, Multiscalar investigation of the Mothra Hydrothermal Field, Endeavour Segment of the Juan de Fuca Ridge, EoS Transactions, Amer Geoophys. Union, 79, 810.

Lerner, G., Whitcomb, L. 1999a, Acoustic micro-bathymetry data processing and rendering software, Technical Report, Dynamical Systems and Control Laboratory, Dept of Mech Eng, Johns Hopkins University, 1999

Lin, C.F 1991., Modern Navigation, Guidance, and Control Processing, Prentice Hall, 1991

Singh, H., Whitcomb, L.L., Yoerger, D., Pizarro, O. 2000, Microbathymetric Mapping from Underwater Vehicles in the Deep Ocean, Journal of Computer Vision and Image Understanding, Vol. 79, No. 1, pp. 143-161, 2000.

Stewart, W. K. 1987, Computer Modelling and Imaging Underwater, Computers in Science, Vol. 1, No 3, 1987, pp. 22-32.

Stewart, W. K. 1990, A Model-Based Approach to 3D Imaging and Modelling Underwater, Trans ASME, Vol 112, Nov. 1990, pp. 352-356.

Stewart, W. K., Multisensor Visualization for Underwater Archaeology, IEEE Computer Graphics and

Applications, March 1991, pp 12-18.

Whitcomb, L., Yoerger, D.R., Singh, H., Mindell, D. 1998, Towards Precision Robotic Maneuvering, Survey, and Manipulation in Unstructured Undersea Environments, Robotics Research - The 8th Int. Symposium, Chap. 2, pp. 45-54, Springer-Verlag, London, 1998

Whitcomb, L., Yoerger, D.R., Singh, H 1999, Advances in Doppler-Based Navigation of Underwater Robotic Vehicles, Proceedings IEEE International Conference on Robotics and Automation, Detroit, Michigan, May 1999.

Yoerger, D.R., Mindell, D. 1999a, Performance of the Exact Subsea Navigation System, WHOI Tech Report, January 1999.

Yoerger, D.R., Kelley, D.S., Delaney, J. R., 1999b, Fine-Scale Three Dimensional Mapping of a Deep-Sea Hydrothermal Vent Site Using the Jason ROVSystem, Proc. Field and Service Robotics 99, Carnegie-Mellon University

.

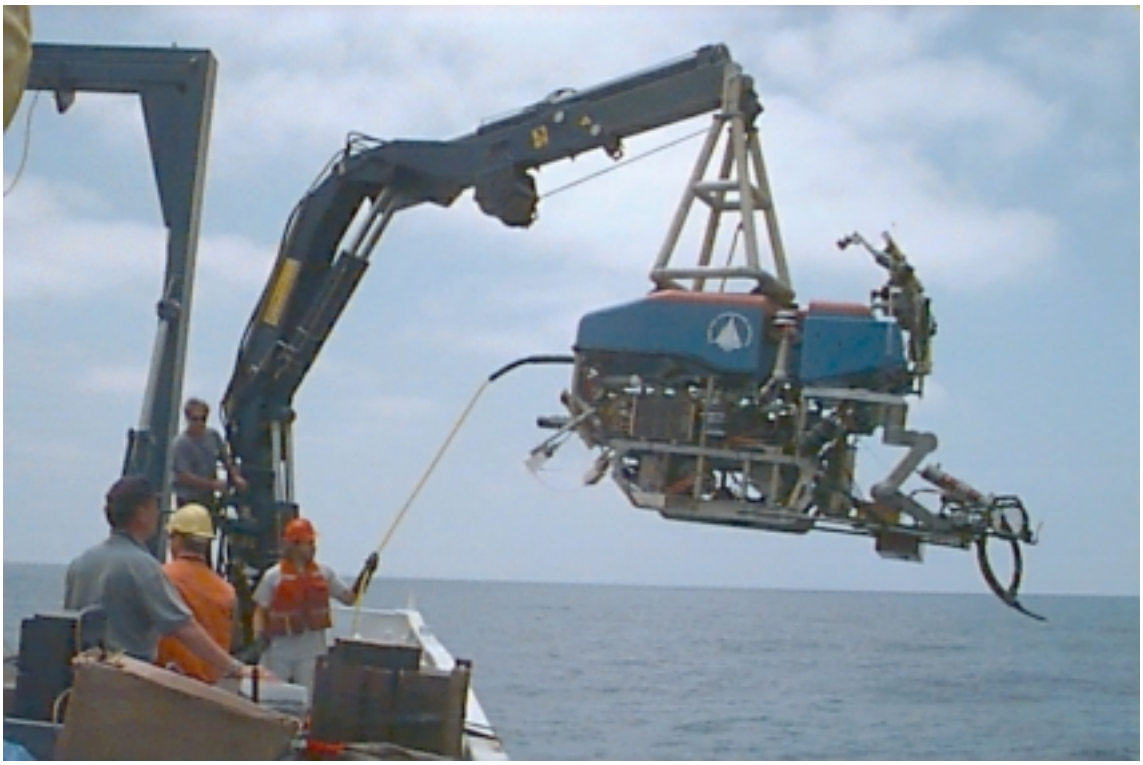

Figure 1. This photo shows the Jason Remotely Operated Vehicle being launched on a recent expedition. The vehicle features a precision navigation suite, an automatic control system, and carries a variety of

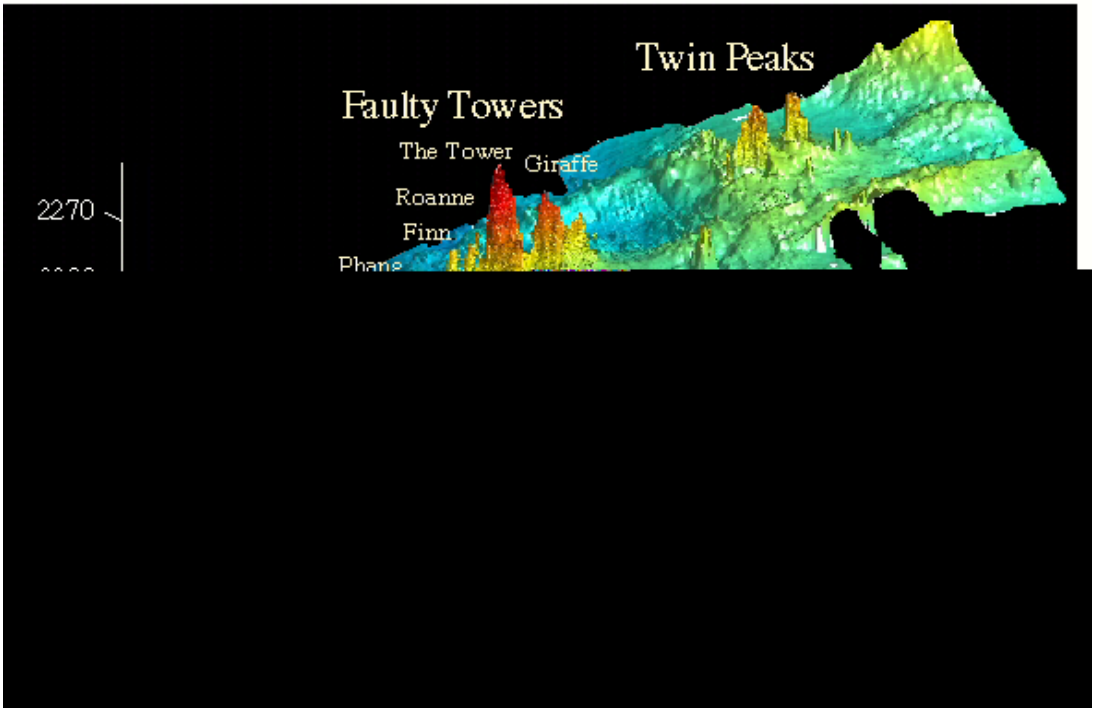

Figure 2. This shows the overall survey result for the Mothra site. The large collection of spires on the left side are called “Faulty Towers”, while the “Twin Peaks” lie to the right side. Other features include other smaller clusters of spires, rugged talus, and the edge of a drained lava lake. The site also contains numerous “black smoker” vents, which emit superheated, mineral laden water.

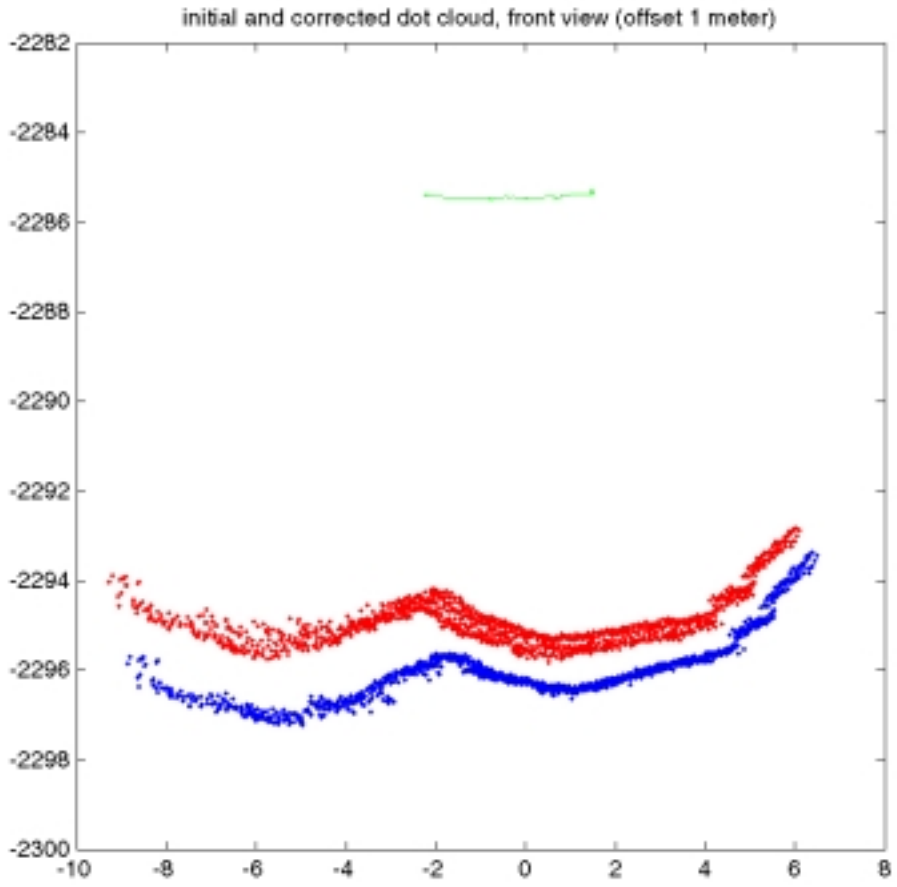

Figure7 This plot shows an example of our use of precise track following to make systematic biases observable. The figure shows a "dot cloud" produced during a slow, sideways motion of the ROV at constant depth over gentle terrain as viewed from behind the vehicle.The sonar data and vehicle track (green trace at the top) have been transformed into a vertical plane parallel to the ROV motion. The "dot clouds" before and after roll correction are shown (offset for clarity). A numerical minimization determined the roll offset that minimized the vertical scatter of the data. The error metric minimized was computed from the sum of the standard deviation of the sonar depth data in each of 50 horizontal bins. The final, processed trace features correct slopes and reduced scatter.

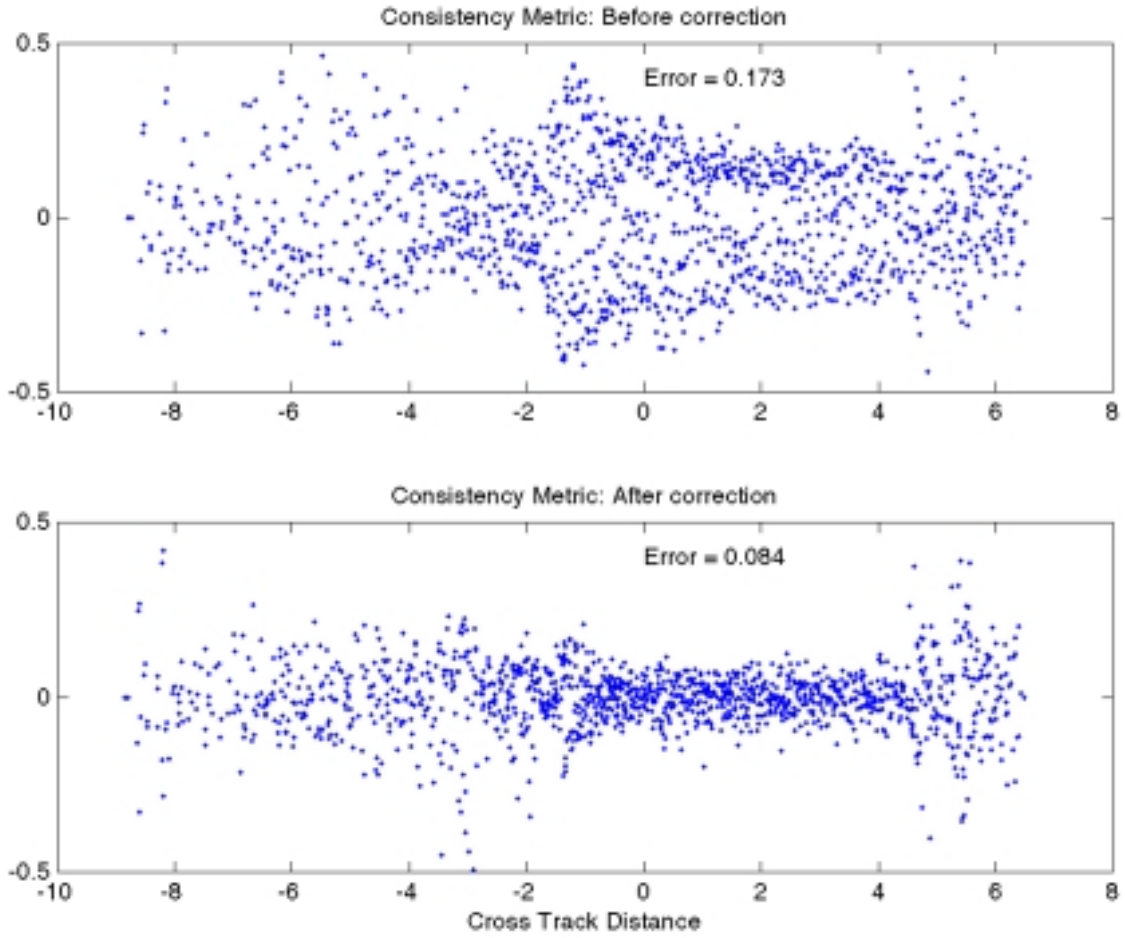

Figure 8. These plots show the error metric used for the roll correction. The upper plot shows the processed profile from the data before correction, which has been sorted into 50 cross track bins, then the mean from each bin removed. This amounts to a spatial high-pass, but can deal with the nonuniform sampling in the cross-track dimension. The lower plot shows the same metric after the roll bias estimate has been adjusted to minimize the error.

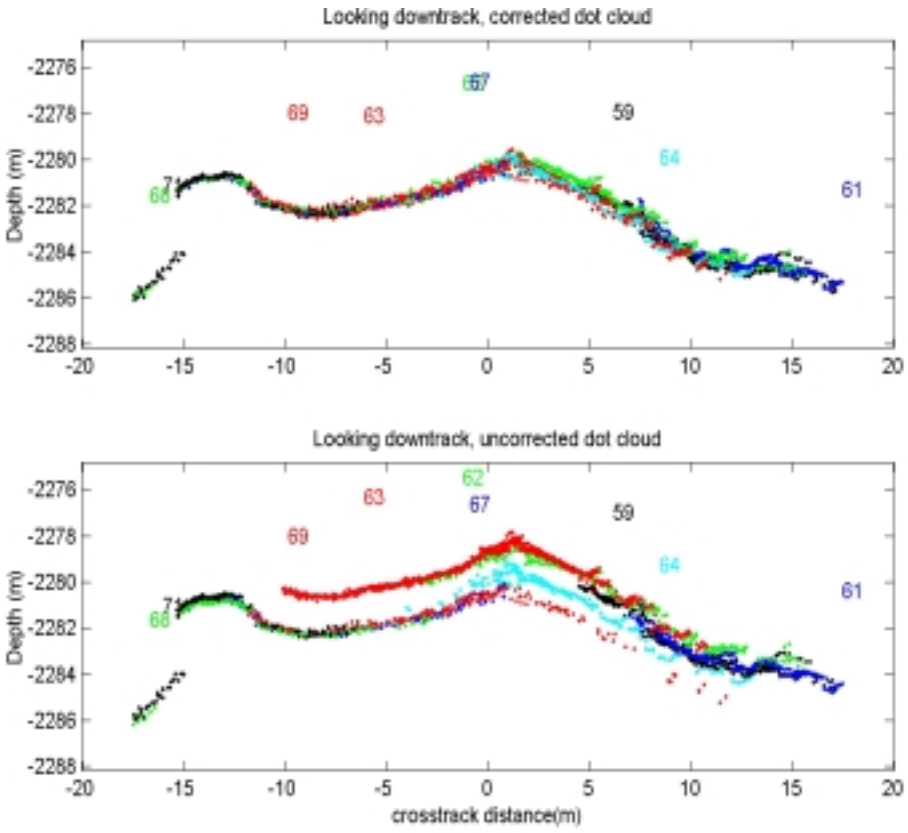

Figure 9. These plots show a one-meter thick vertical slice of the downlooking sonar data, before and after a depth correction was computed for each transect. The numerals refer to transect numbers. Individual depth corrections were computed by performing a sequence of 1-parameter minimimizations using the same error metric as for the roll correction.

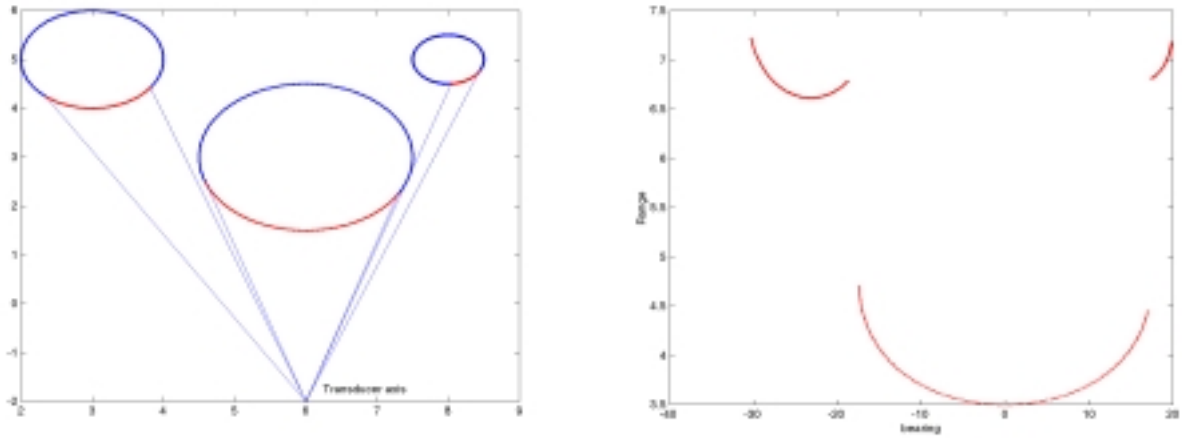

Figure 10. For processing the vertical transects, we processed the data in cylindrical coordinates to take advantage of Jason's precise control and the intrinsic geometry of a scanning sonar, reducing much of the processing to two-dimensions. For each value of angle and height, only one value exists in the radial direction. This permits greatly simplified spatial filtering, gridding, triangularization, and segmentation.

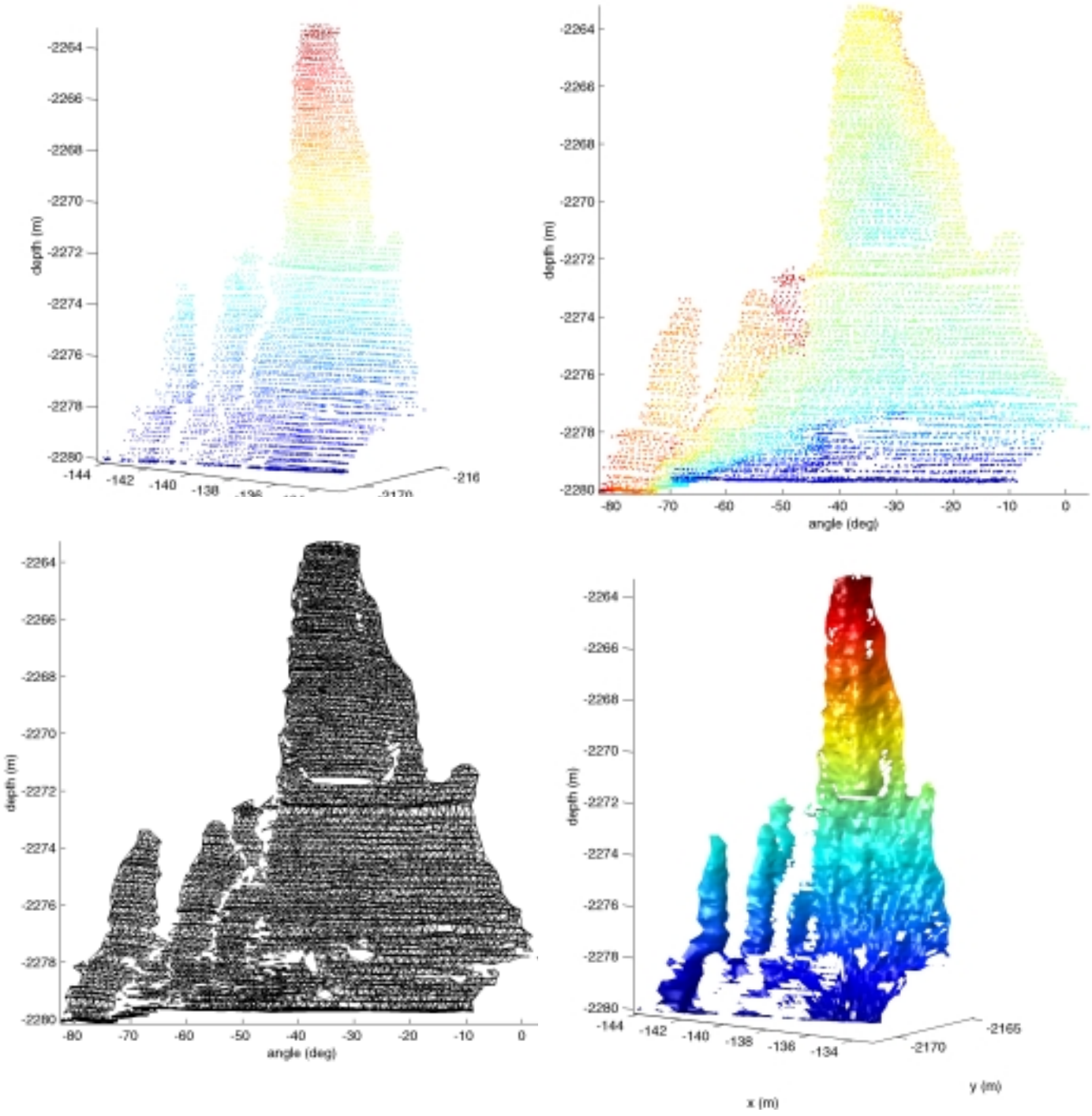

Figure 11. These plots show how the forward-looking sonar data for a single vertical transect was processed. The example shows the east face of the spire called "The Tower" , the largest of the structures in the Mothra field along with three smaller spires . The upper left panel show the raw 3D sonar "dots", colored by depth. The upper right panel shows the transformation into cylindrical coordinates, with color representing the radial direction. The lower left panel shows the triangulated and segmented surface. In cylindrical coordinates, overlapping structures are not blurred together and are easily separable without resorting to fully 3D processing. The lower right panel shows the surface transformed back into world coordinates, colored by depth, and illuminated.

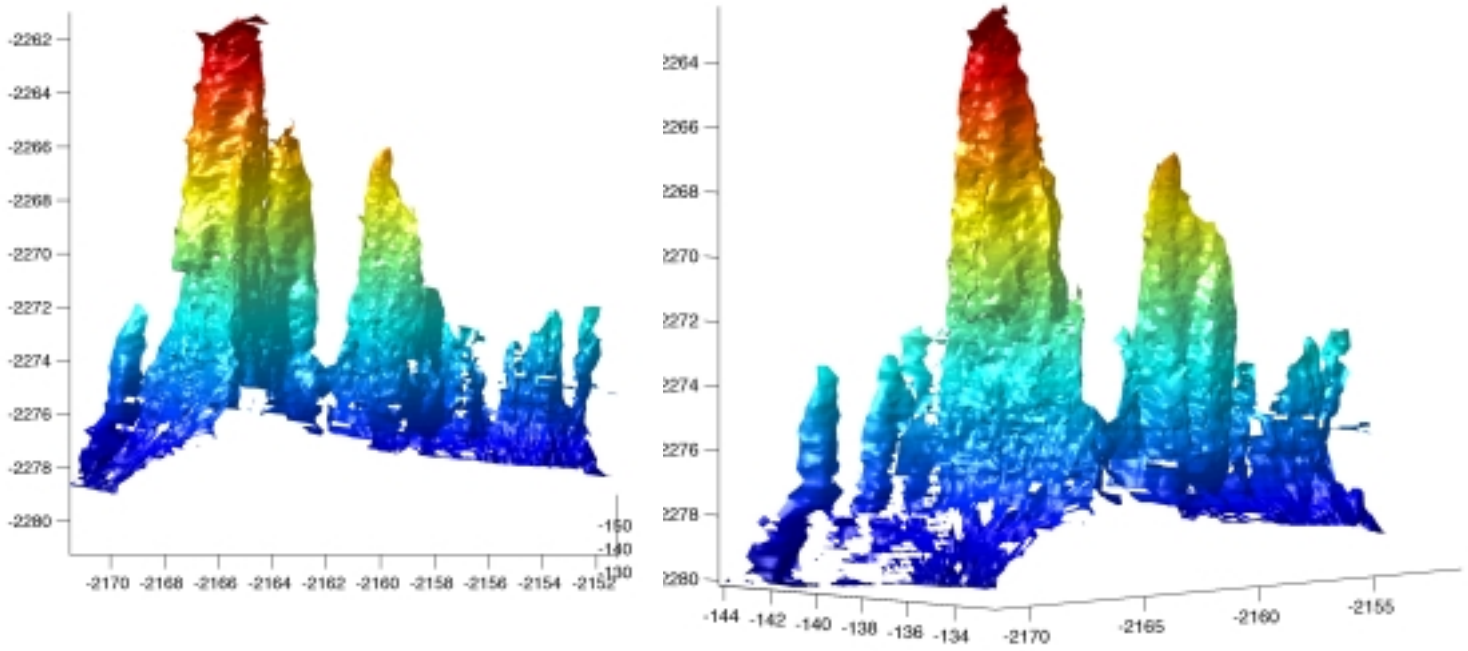

Figure 12 These plots show two views of the east face of the Faulty Towers complex as imaged with the scanning sonar in the forward looking configuration using data from eight transects. Three smaller spires can be seen on the left side, and the rightmost feature is a hot water plume. The large nose-like "flange" structure on Tower can be clearly seen in the left view.

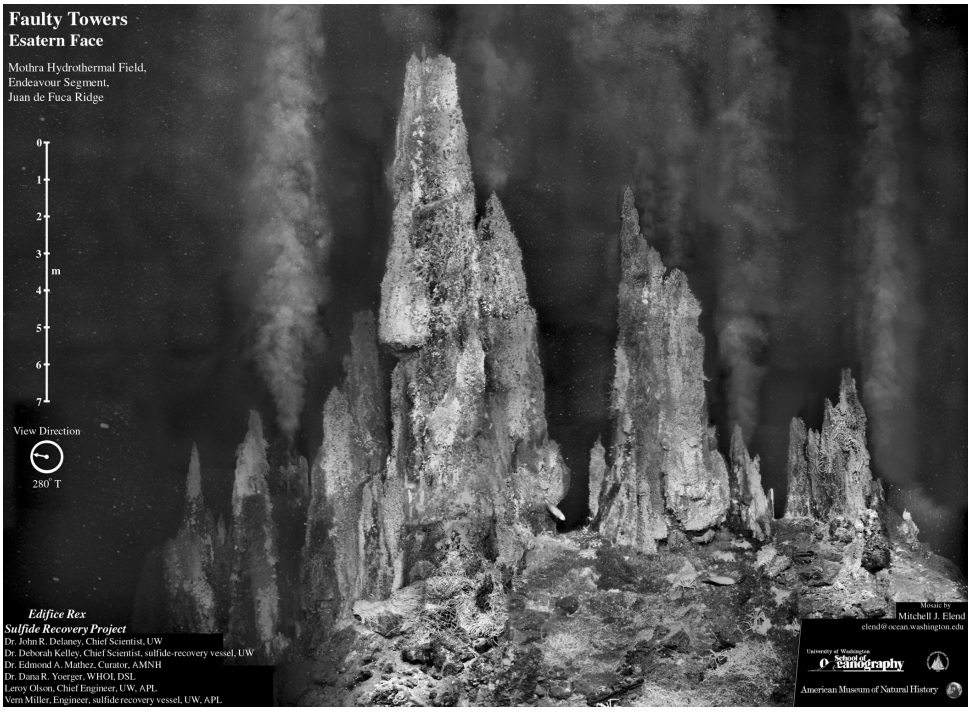

Figure 13 This photomosaic of Faulty Towers as viewed from the east was assembled from 67 electronic still camera images. Precise vertical track-following and careful transect planning greatly simplified the mosacking process and improved the quality of the final product.

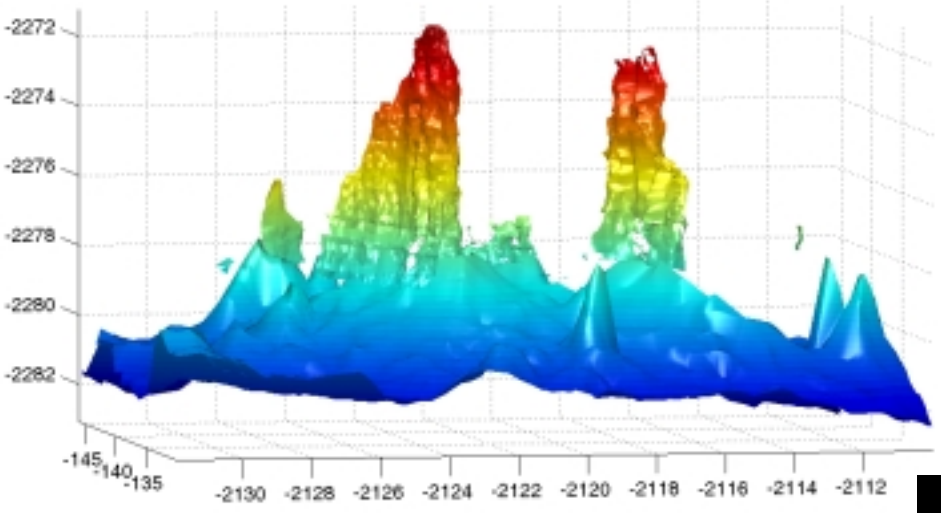

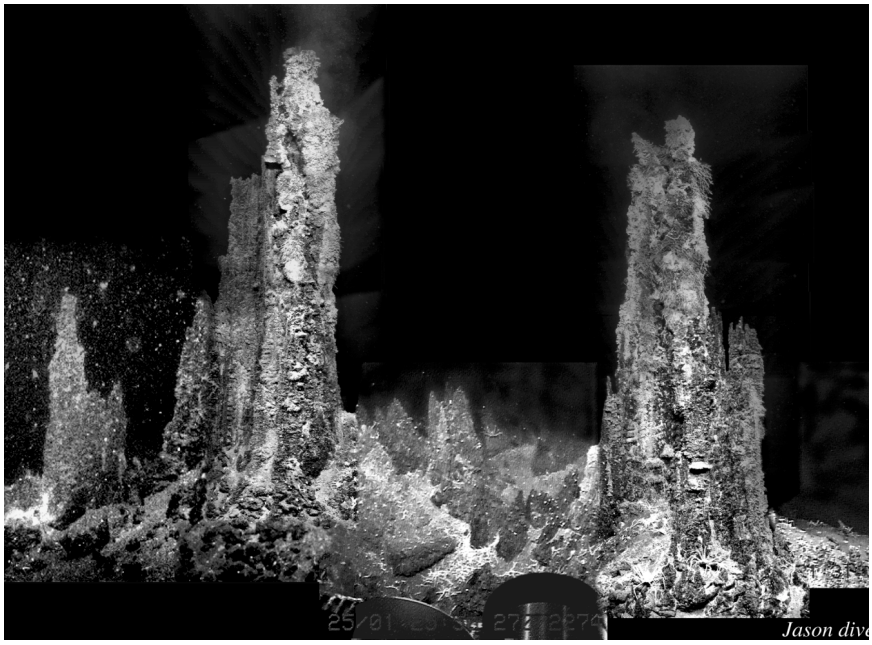

Figure 14 These plots show three renderings of the Twin Peaks complex, located about 50 meters north of the Faulty Towers complex. The upper panel shows the rendering from the sonar in the forward looking configuration combined with the down-looking data. The lower left panel shows a photomosaic assembled from over 20 electronic still camera images, and the right panel shows a closeup of the rightmost tower Flying Buttress assembled from 7 digitized 35mm still images.

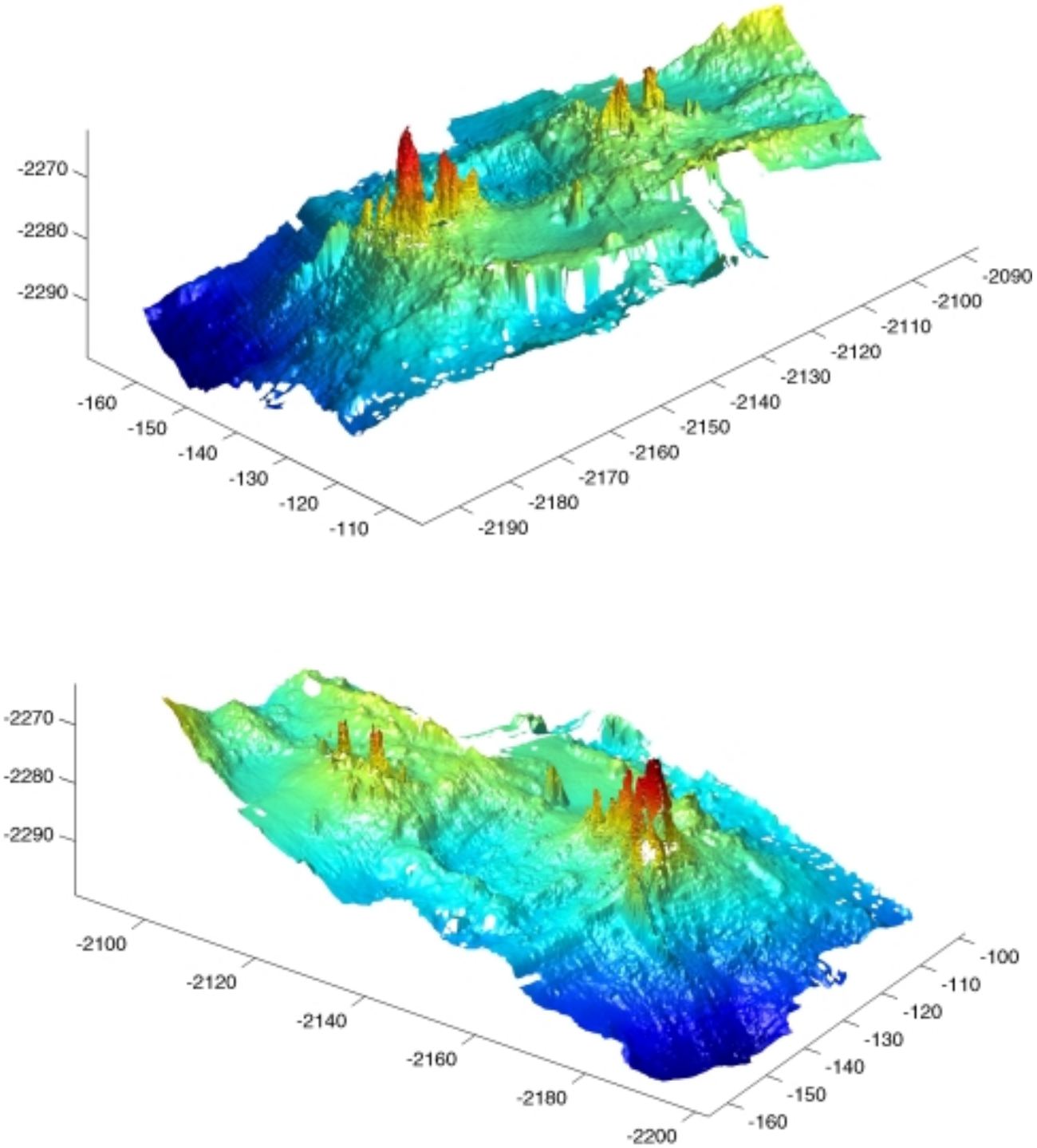

Figure 15 These plots show scanning sonar data assembled from 18 downlooking and 34 forward looking transects. The Faulty Towers complex is the larger group, Twin Peaks is the smaller pair of structures. Downlooking data was spatially filtered using a gaussian kernel with a sigma = 0.20 meter The forward looking data, gathered at finer resolution, was filtered with a value of sigma = 0.05 meter.